Supplement.

Apparatus details….

PhoFR is a jacketed flow reactor with 5.0 cm inner diameter, with 110 cm of its length illuminated by 4 BLB fluorescent bulbs. Most gas inlets are located in a conical region partitioned from the main flow reactor by a Teflon mesh (~ 0.5 mm x 0.5 mm openings); the base inlet is located just below this mesh. A phosphoric acid coated 80 cm length of tubing – along with a thin strip of Teflon mesh to maintain acid spreadout – was installed on the exit of the dry N_2 flow meter (23Aug2019). Algae accumulation inside the cooling jacket was almost completely removed (alcohol - KOH soak) in Dec2019. Neither of these actions had noticeable effects on the temporal trends in experimental results.

The second particle counter is the UCPC system used in Zollner et al. [2012] which is nearly identical to that described by Stolzenburg and McMurry [1981]. The new working conditions for this instrument presented by Kuang et al. [2012] was used for the work here: saturator temperature of 45 C, condenser temperature 10 C, condenser flow of 10 cm^3/s (0.6 Lpm) and a capillary flow of 1.2 cm^3/s. The 50% cutoff diameter for these UCPC conditions is ~2 nm. A transport flow of 0.3 Lpm was used for the majority of the measurements, due to limitations of the total flow in the experiment. The effect of transport flow on the UCPC count rate is shown in Fig. S1 below (the 0.6 lpm data was collected with a decreased DEG transport flow.)

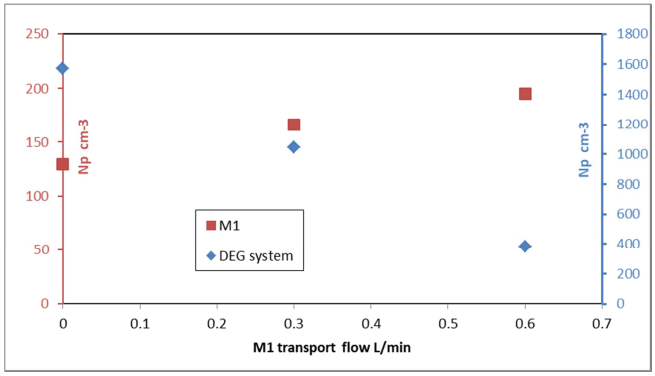

Fig. S1. N_p vs. M1 (a UCPC) transport flow rate. The sampling rates of the DEG system and M1 were unchanged with transport flow. The DEG transport flow was lowered from 1.5 to 1 L/min for the data point at 0.6 L/min. Exp. Conditions: Q_4=1.84 sccm, 220 ppt NH_3 added, D_{le} for particles was 3.2 nm. (2020jan29) Note that a much larger effect was discovered when UCPC data appeared to be affected by a contaminant (see next section.)

Variation of N_p with relative humidity for UCPC and DEG measurements.

A set of results for Q_4 = 4.2 sccm where relative humidity was varied by setting the flow through the humidifiers (0.69 to 2.36 sLpm; about 24 to 81 % RH.) Both particle counters were elevated compared to apparatus floor due to a recent gas-source change but the UCPC numbers had increased the most, over their floor by as much as an order of magnitude. When this data was taken, UCPC results generally trended higher than the DEG results. This could be due to (i) changes in how the sampling flow was split between the instruments and (ii) restricting DEG N_p to the leading edge particles and (iii) the episodic contamination may have influenced differently the UCPC and the DEG counting efficiencies. For (i), the flow splits at a ¼" Swagelok tee with the UCPC sampling straight and the DEG taking its flow at right angles: while early experiments showed little difference between them when the DEG sampled straight, things may have changed. For (ii) small particles in the DEG distributions can number as much as that in

the leading edge. Evidence for any or all of these occurring is a recent large dependence of UCPC count rates on UCPC transport flow rate, much larger than is exhibited in Fig. S1.

Nonetheless, both sets of N_p data are much lower than our previous results with the largest difference at high RH. The difference between the DEG and UCPC results decreases at low RH which may be for the same reason the DEG Np is higher at low Q_4: the DEG system may be detecting ion-molecule clustering reactions in the charger, as discussed in the paper.

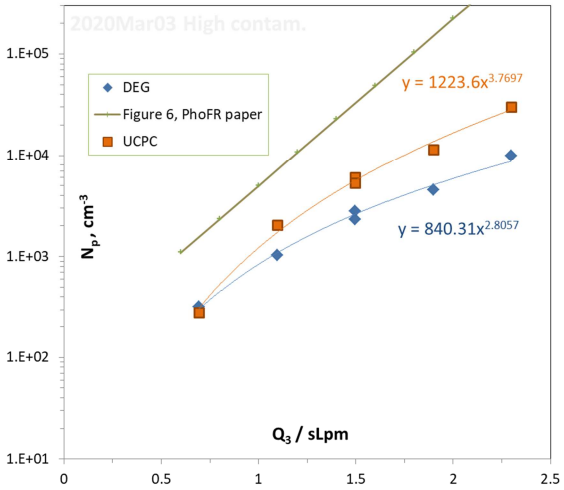

Fig. S2. Comparison of the RH dependency at Q_4=4.2 sccm for the present measurements (DEG and UCPC) to PhoFR previous data (gold line).

<u>Room temperature variations.</u>

An example of an incident where a fluctuation in the temperature of the top cone (T_{cone}, red line) affected the UCPC ("M1 rate") and the DEG system measurements (raw count rates for several voltages sent to the nano-MPS are shown).

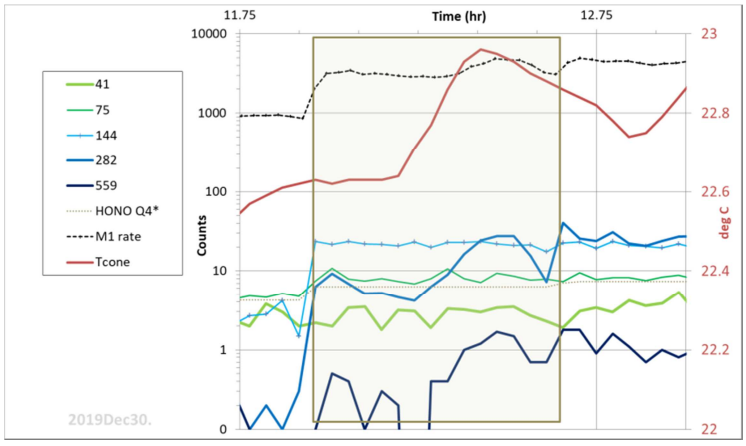

Fig. S3. Plots of particle detector count rates (left axis) and T_{cone} (right axis) vs. time. The gold box highlights the data while Q_4 was constant at 6.3 sccm.

Attempts to see effects on N_p by intentionally varying T_{cone} were not conclusive. We think changes in T_{cone} are a proxy for changes in the temperature of the room that may have affected the temperature of another part of the apparatus, such as the reservoirs and delivery lines for the HONO source.

External particles grown in PhoFR.

Additional experimental results for the growth of nanoparticles introduced at the top of PhoFR as a function of Q_4, the flow through the HONO source. The particle size distribution volume-weighted diameter is plotted vs. Q_4 in Figs. S4 and the particle's initial size is indicated at Q_4 = 0 (determined from the lights off measurements.) Shown in Fig. S5 are the size distributions for one set of measurements.

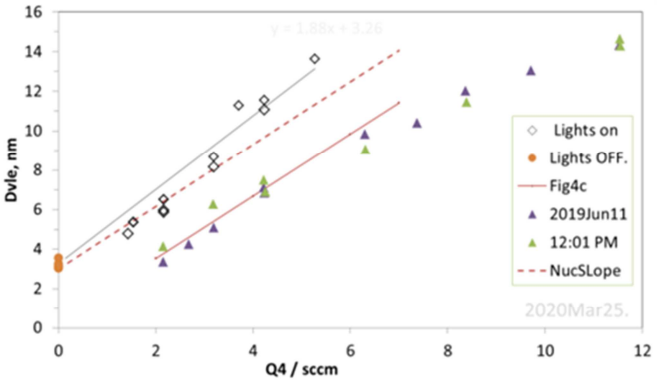

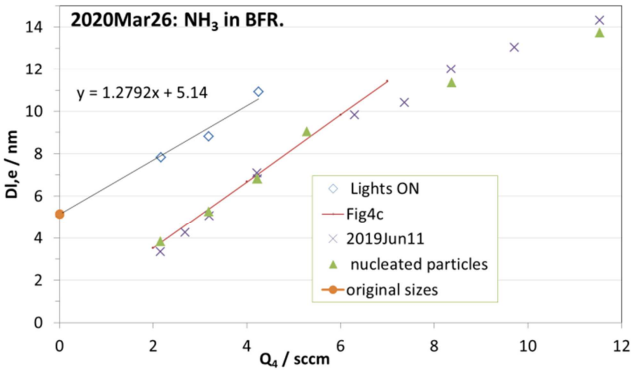

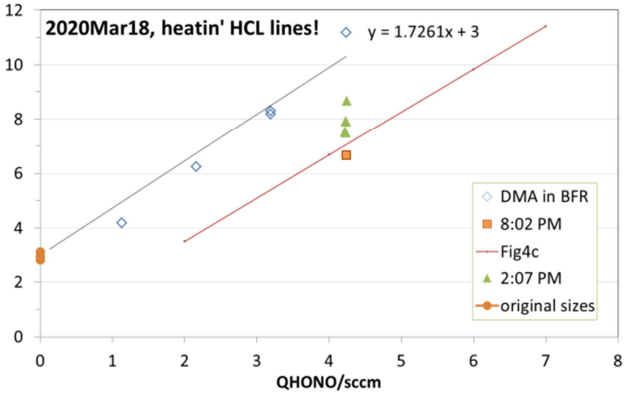

Fig. S4. Volume-weighted diameter of particles vs. Q_4, the HCl-laden N_2 flow through the HONO source. Data at Q_4=0 are the initial size of the nanoparticles (orange circles, with photolysis suspended).

(a) The green triangles and purple symbols are representative data for nucleation of particles in PhoFR from 2020Mar25 and 2019Jun11, resp., (N_p was $3x10^4$ cm^{-3}.) The growth slope is somewhat larger than the nucleation slope.

(b) Nanoparticles produced in BFR with ammonia at 1.3 ppbv. The growth slope is lower for this set of data. The nanoparticles are more numerous ($2x10^5$ cm^{-3}) and their size distributions were not well-described by a single log-normal:

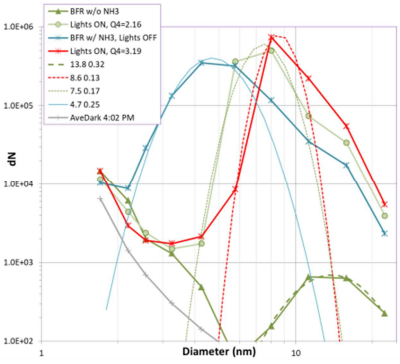

(c) The upper portion of the HCl-source and the lines leading to the NaONO(s) vessel were gently heated for this data and HONO level (and perhaps NO) was elevated: the green triangles are sizes for nucleation of particles in PhoFR for that day, also slightly elevated. N_p was $3x10^4$ cm^{-3}.

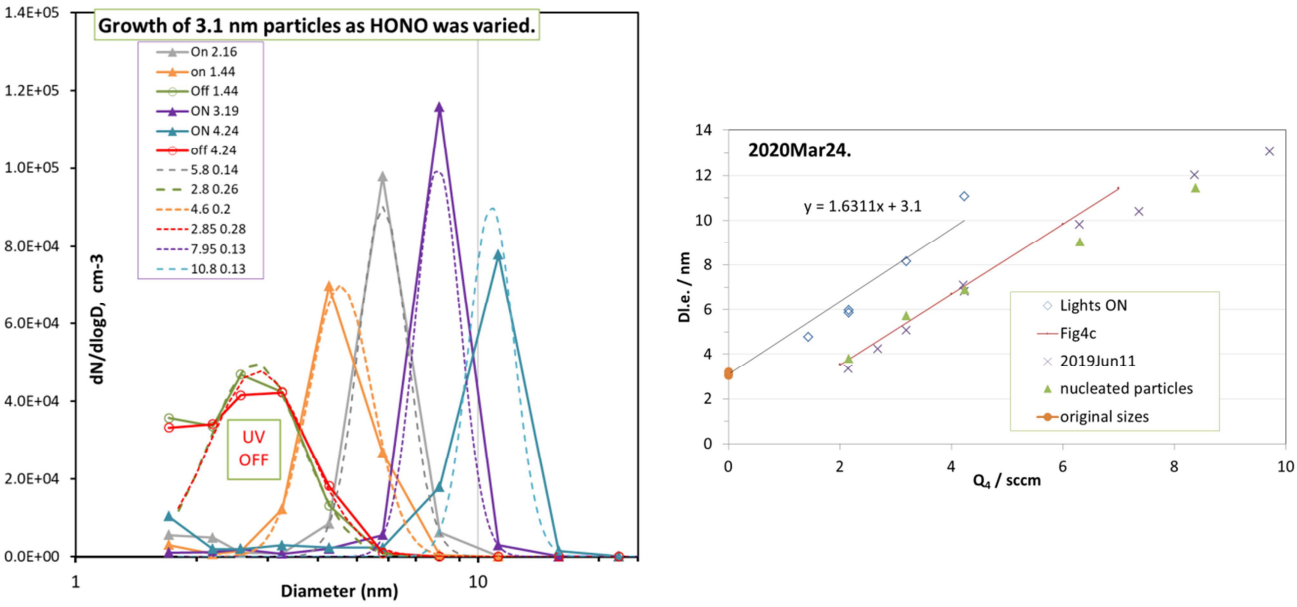

Fig. S5. Growth of nanoparticles. (a) size distributions as a function of HONO flow; lights OFF distributions are in green and red (2020mar24 data.) Initial particles generated in BFR (Glasoe et al.) with 15 ppt DMA and a very low total flow (1.5 sLpm). (b) Growth plots for this data, as in Fig. S4a-c.

Model details.

The model is explained in Hanson et al. [2019] and here significant changes in parameters are detailed. The main differences are in the HONO and NO levels. The HCl mole fraction of Q_4 is now 12.8 ppbv (notwithstanding small fluctuations in total pressure) which was taken from the slope of the NO_x versus Q_4 measurement (Fig. 2); this is about a 15 % decrease from our previous estimate. The NO level is taken from the measurements shown in Fig. 2; NO_2 is taken to be equal to NO and HONO is summarily reduced. The inclusion of initial NO levels from the HONO source is the most consequential difference with our previous model calculations.

No longer included is a reaction between HO_2 and SO_2. It had been invoked to explain the dependence of N_p on SO_2 level in our previous work. This reaction added 10-15 % to the simulated H_2SO_4 production rate. Interestingly, with the inclusion of small amounts of NO and NO_2 coming from the HONO source, the model (with 20 pptv ammonia, Fig. S6) shows a significant dependence on SO_2 level which may be due to SO_2 competing with NO and NO_2 for OH.

There are a few other model details worth re-iterating here. When a base is added, it is constrained to the middle 25 % of the mass-flow (middle fake) to mimic the elevated concentration of the base in the sidearm flow in the experiment. All temperatures are 296 K and laminar flow is assumed. N_p is taken to be the sum of all the truncation clusters at Z=120 cm and R = 0 when clusters were limited to 10 SA molecules; when growth to larger clusters was simulated, Np is the sum of all clusters of 10 or more SA molecules.

UCPC and DEG N_p as a function of SO_2.

Three sets of calculations and two sets of experimental data are shown in Fig. S6 where SO_2 was varied (Q_1 is flow of the 1% SO_2 in air mixture) at Q_4 = 4.2 sccm. The NH3_D52 (aka D52octo)) model results for zero ammonia (purple line) and 25 pptv ammonia (orange line) do not describe the data very well. If a strong nucleating agent that acts like dimethylamine is present at 10^{-16} mole fraction, the model results with DMA_I free energies [Hanson et al. 2017] results best approximate the lack of a dependence on SO_2 in the data.

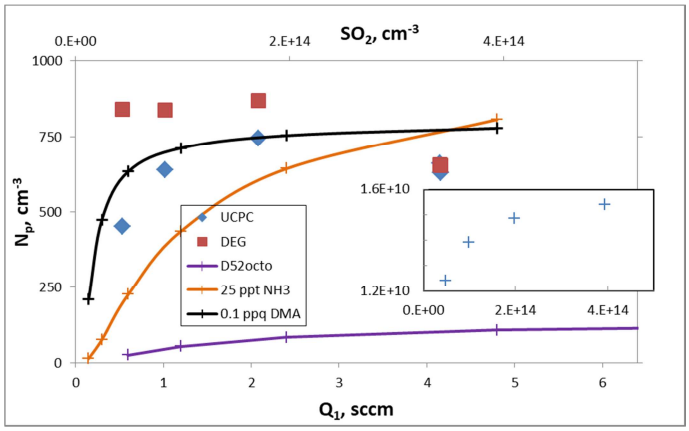

Fig. S6. Variation of N_p with SO_2 flow rate. 1 sccm of the 1 % SO_2 mixture is a number density [SO_2] of 8.6×10^{13} cm^{-3}. Many of the previously published experiments from PhoFR showed a large effect with N_p increasing from 7000 cm^{-3} to 30000 cm^{-3} over the range of SO_2 in Fig. S6. Inset shows on-axis [H_2SO_4] at 120 cm as a function of [SO_2]

Growth rate calculation.

Sulfuric acid-water nanoparticles' composition is predicted to vary with size (see Table S2, Liquid Drop Model [Lovejoy et al. 2004; Yu et al. 2005]) and therefore the Verheggen and Mozurkewich [2002] approach, where the particle's volume is differentiated with respect to time, is a good starting point. After we modify it by including some terms and rearranging it, we will integrate it from 2.2 to 8.7 nm (geometric or mass diameter.) This equation is readily modified to account for the vapor molecule's size (parenthetical term in S1) and for the particle–vapor reduced mass (in the mean molecular speed $\bar{c}_r$) (see Niemenen et al. [2010] for a similar modification). Many variables are then incorporated into a collision rate coefficient k_{GR}.

$$\frac{dD_p}{dt} = \frac{M_{SA}\alpha\bar{c}_r[SA^*]}{N_A 2w\rho}\left(1+\frac{d_{vapor}}{D_p}\right)^2 - \frac{D_p}{3}\frac{d\ln w\rho}{dt} \qquad \text{(S1)}$$

$$= k_{GR}[SA^*] - \frac{D_p}{3}\frac{\partial \ln w\rho}{\partial D_p}\frac{dD_p}{dt} - \frac{D_p}{3}\frac{\partial \ln w\rho}{\partial RH}\frac{dRH}{dt} \qquad \text{(S2)}$$

Here, D_p, w and ρ are the particle's diameter, SA (sulfuric acid) weight fraction, and density, respectively; M_{SA} is SA's molar mass, N_A is Avogadro's number, α and $\bar{c}_r$ are the mass accommodation coefficient of SA and mean molecular speed (using the reduced mass, taking into account hydration, Hanson and Eisele [2000]; about 2 water molecules at 52 % RH), [SA*] is the concentration of SA molecules and its hydrates, and d_{vapor} is the average diameter of hydrated SA molecules, 0.64 nm. Note that $\bar{c}_r$ calculated using the reduced mass of the particle-SA* collision for a particle diameter of 2.2 nm is only 1.35 %

greater than the mean molecular speed of SA_1W_2. k_{GR} subsumes all the parameters besides [SA*] in the first term of the RHS of the top line.

$$k_{GR} = \frac{M_{SA}\alpha\bar{c}_r}{N_A 2w\rho}\left(1+\frac{d_{vapor}}{D_p}\right)^2 \qquad \text{(S2b)}$$

Solving for dD_p/dt for these conditions yields:

$$\frac{dD_p}{dt} = \frac{k_{GR}[SA^*] - \frac{D_p}{3}\frac{\partial w\rho}{\partial RH}\frac{dRH}{dt}}{1+\frac{D_p}{3}\frac{\partial \ln w\rho}{\partial D_p}} \qquad \text{(S3)}$$

The last term in the numerator is zero for experiments at constant RH and

$$\frac{dD_p}{dt} = \frac{k_{GR}[SA^*]}{1+\frac{D_p}{3}\frac{\partial \ln w\rho}{\partial D_p}} \qquad \text{(S4)}$$

While k_{GR} accounts for uptake due to SA molecules it also accounts for water molecules taken up in addition to those attached to the SA molecule, determined by the nanoparticle's composition and density. The denominator accounts for additional water molecules taken up as the particle's composition changes with size. For the present conditions, this latter effect is about 8 % over the 3 to 8 nm range (i.e., the denominator is 0.92). See Table S1 below for representative values for the size dependent terms.

Splitting the growth from 2.2 to 8.7 nm into three time intervals Δt_i of 7.5 s to obtain an average value for k_{GR}/denominator of 3.38×10^{-11} nm cm^3/s, an average H_2SO_4 concentration is estimated from equation (S4)

$[SA^*]_{ave}$ = 6.5 nm / (22.5 s * 3.38×10^{-11} nm.cm^3/s)=8.55×10^9 cm^{-3}.

More rigorously, using the H_2SO_4 concentrations on-axis shown in Fig. S7 below (blue +) and calculating $\Delta D_p = \Sigma\,(dD_p/dt)_i\Delta t_i$ from i=1 to 3 using the values in rows 2,3 and 5 in Table S1 we get an increase in diameter of 6.8 nm. This simulation used a photolysis rate for HONO of 6.7×10^{-4} s^{-1}, which may be about 5 % too large based on this growth rate calculation.

D_p (nm)	**W**	**ρ (g/cm^3)**	**wρ**	**k_{GR} (10^{-11} nm cm^3/s)**	**1/den. (S3)**	**Est. time (s)**	**Average [H_2SO_4] / cm^{-3} In time interval**
2.2	0.58	1.47	0.85	3.44		0	
3.3	0.54	1.44	0.78	*3.30*	1.077	*7.5*	*2.7e9*
5.0	0.51	1.40	0.71	3.13	1.094	15	1.01e10
7.7	*0.66*	*1.38*	*0.66*	*3.11*	*1.08*	*~19*	
8.7	0.65	1.375	0.65	3.08	1.058	22.7	1.45e10
10.0	*0.64*	*1.37*	*0.64*	*3.06*			

The calculation of ΔD_p: 7.5*(3.30e-11*1.077*2.7e9 +3.13e-11*1.094*1.01e10 + 3.08e-11*1.058*1.45e10).

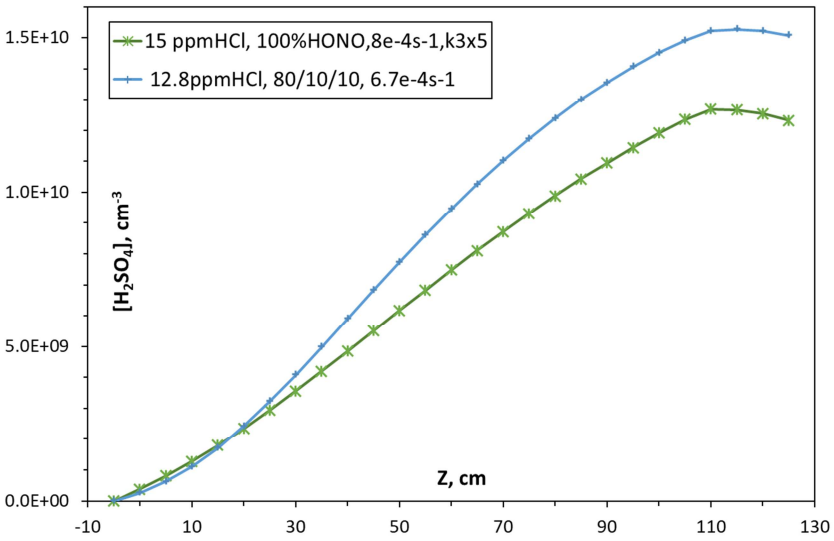

Fig. S7. Comparing Q_4 = 4.2 sccm on-axis H_2SO_4 concentrations simulated with previous parameters (green) [Hanson et al. 2019] and the present ones (blue) where less NO_x enters and 10 % of that enters as NO and there is no reaction for HO_2 with SO_2 (k3x5). The average on-axis $[H_2SO_4]$ from Z=0 to 125 cm for these simulations are (blue +) 8.97×10^9 cm^{-3} and (green *) 7.36×10^9 cm^{-3}.

It is reasonable to suggest that a more appropriate measure of the particles' exposure to H_2SO_4 is the mixing-cup concentration: a flow-weighted average over the region sampled by the DEG system, 2 L/min. Assuming the DEG system samples the middle of the flow, this region covers radii from 0 to 1.4 cm. Shown in Fig. S8 are (a) the radial distributions of $[H_2SO_4]$ at four axial distances and (b) the mixing cup and on-axis $[H_2SO_4]$. Averaged from 0 to 120 cm, the mixing-cup concentration is about ten % less than the on-axis concentration. Since half of this is the 5% difference discussed in the previous paragraph, we use the 6.7×10^{-4} s^{-1} value for the HONO photolysis rate.

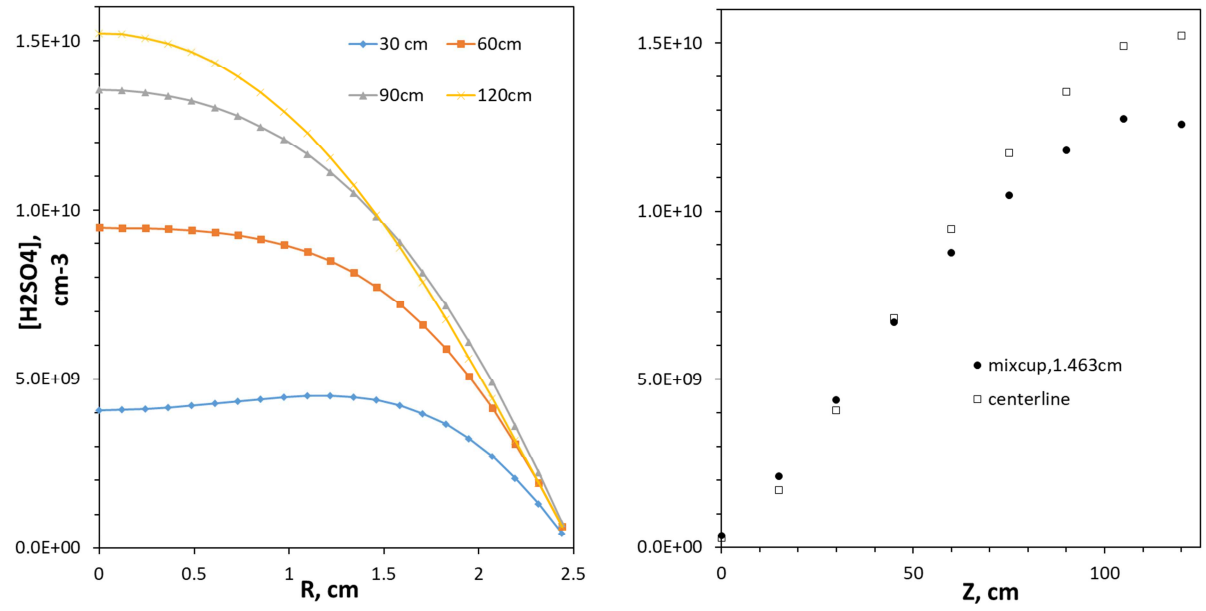

Fig. S8. Simulated $[H_2SO_4]$ at Q_4 = 4.2 sccm. (a) Radial distributions at a few axial distances. Note that the data for Z = 120 cm is 20 cm beyond the simulation's lighted section. (b) Mixing-cup concentration and on-axis (centerline) concentrations plotted vs. axial distance.

Lastly, the green asterisks plotted in Fig. S7 are the simulated values using the previous values from Hanson et al. [2019]. These values differ from the present: 15 ppm HCl level in Q_4, no initial NO from the HONO generator, a photolysis rate of $8x10^{-4}$ s^{-1}, and a reaction between HO_2 and SO_2 was assumed to occur. The $[H_2SO_4]$ averaged along the length of the reactor is $7.36x10^9$ cm^{-3}, about 18 % less than that of the current simulation.

Previous determination of H_2SO_4 concentration: Photolysis rate, dependence on Q_4, etc.

Isoprene and methylvinylketone/methacrolein measurements were used to estimate the amount of HONO oxidized in our previous work [Hanson et al. 2019], however, the presence of 10 % NO was not considered. Again, the other differences are: (i) a level of 15 ppmv for the HCl-in-N_2 flow was estimated in our earlier work that leads to higher calculated HONO, (ii) also included was a reaction between HO_2 and SO_2 that yielded H_2SO_4 and an additional OH molecule and (iii) the HONO photolysis rate was larger. The HONO photolysis rate was estimated from absorption measurements along with isoprene photo-oxidation experiments, from the relative amount of methylvinylketone and methacrolein produced per isoprene lost. The precision of the absorption measurement was low and the presence of NO_2 was not well quantified and was thought to be due to HONO decomposition in the absorption apparatus. Nonetheless, the old photolysis rate is within 20 % of that estimated here. The difference in the calculated H_2SO_4 between the simulation then and the present simulations is only about 20 %, well within the uncertainties of the measurements and in the branching ratios of isoprene's dominant photo-oxidation pathways.

Plots of modeled H_2SO_4 vs. experimental conditions.

Shown in Fig. S9 are simulated H_2SO_4 (on-axis values) (a) averaged over the length of the reactor plotted vs. Q_4 and (b) at four different Q_4, normalized to the value at 120 cm. Figure S9(b) shows how the simulation's axial profile changes with Q_4.

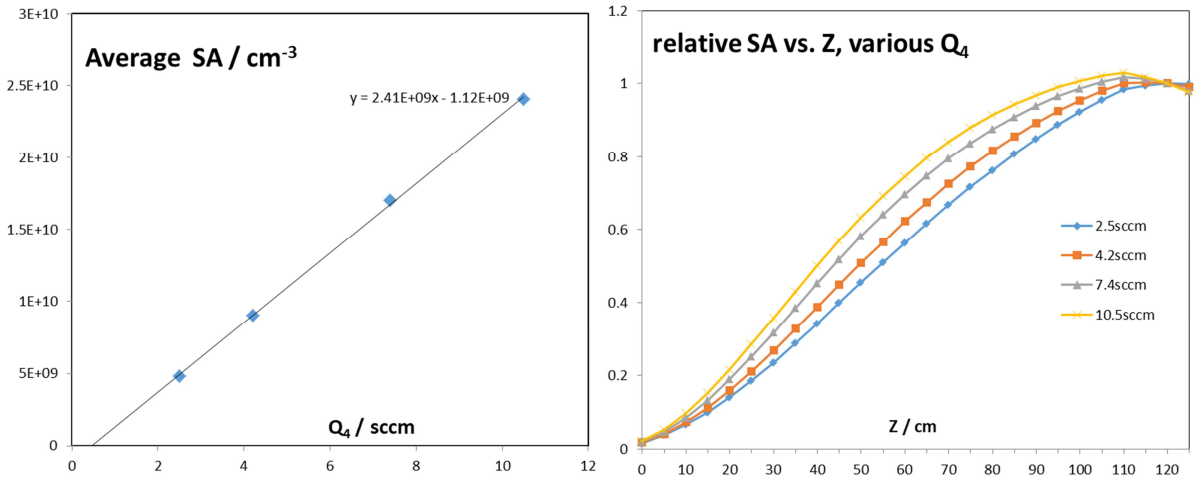

Fig. S9. Modeled on-axis $[H_2SO_4]$. (a) Average value over the length of the reactor vs. Q_4/sccm. (b) H_2SO_4 concentrations vs. axial distance, normalized to their values at 120 cm.

Modeled particle size distributions

Here we present simulated particle size distributions using that option in our model [Hanson et al., 2019]. The model was run with zero-added base conditions to simulate particles formed in the binary system or with small amounts of ammonia or dimethylamine. Q_4 was 4.2 sccm and clusters containing up to 1000 or 2000 H_2SO_4 molecules were simulated with only the first ten allowing for loss of H_2SO_4 molecules. Shown in Fig. S10 are the modeled size distributions on axis at the end of the flow reactor along with two experimental size distributions.

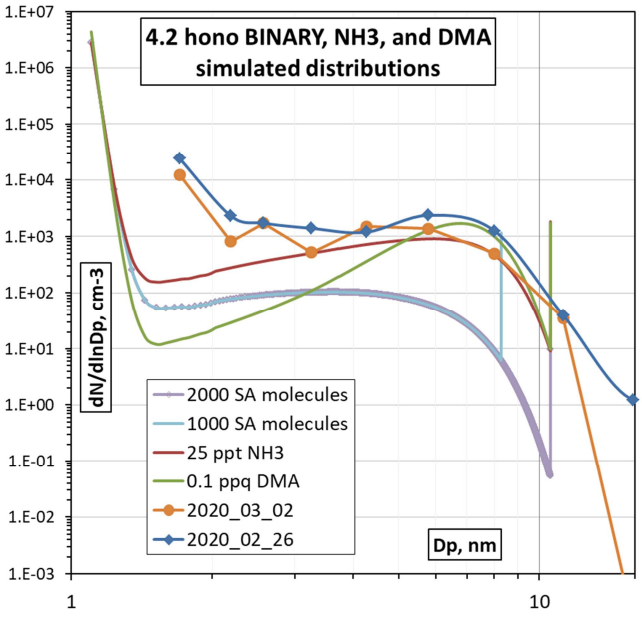

Fig. S10. Size distributions, experimental and modeled for Q_4=4.2 sccm and 52% RH at [R,Z]/cm = [0,120].

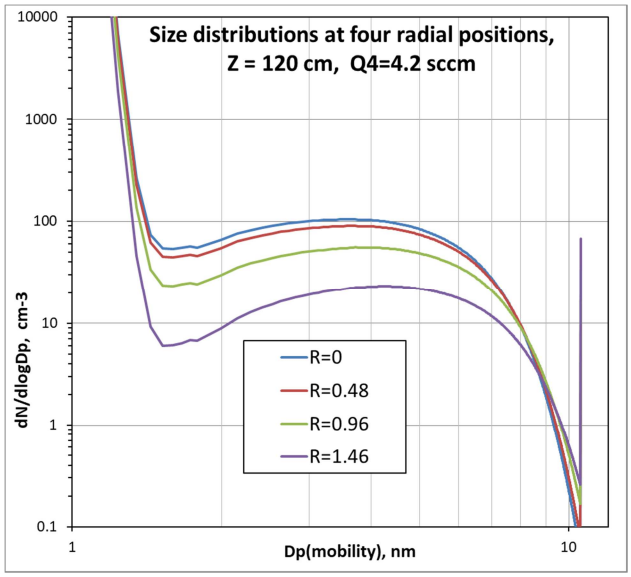

Fig. S11. Modeled size distributions at 120 cm (where particle detectors sample). Four distributions for four radial positions are shown for binary conditions.

The binary simulations compared to the experimental data show a discrepancy in the magnitude of the particle number concentrations, which is consistent with the finding that the DEG data is subject to potential overcounting and particles may be enhanced due to contaminants and/or ion processes. Yet the shape and position (i.e. leading edge) of the binary and experimental distributions are similar. The truncation of the modeled distribution when the clusters were limited to 1000 SA molecules is evident but this has no effect on the other clusters nor on the total number density: the distribution changes very little when the maximum cluster size was raised to 2000 molecules.

Both simulations with the added base capture the leading edge of the experimental distributions very well with the 25 ppt NH_3 simulated distribution best describing the whole of the experimental distribution. Yet a combined scenario where ion-processes dominate for 3 nm and smaller diameter particles (not included in the simulations) and a mole fraction of $1x10^{-16}$ dimethylamine yields the large particle mode is also possible. This combined scenario is supported by the experimental SO_2-dependence (Fig. S6) where a better description was found for dimethylamine than ammonia.

Composition of the nano-particles.

We used the liquid drop model calculations of Lovejoy et al. [2004] to obtain the composition of aqueous sulfuric acid nano-droplets as a function of size for 296 K and 52 % RH. These are shown in Table S2 along with the 298 K and 50 % RH data from Fig. 2 of Yu [2005] for comparison. Note that bulk densities that corresponded to the composition of the nanoparticles were assumed to apply to the nanoparticles. The mass diameter is about 0.3 nm smaller than the mobility diameter according to Larriba et al. [2010].

Table S2. Compositions of H_2SO_4-H_2O clusters from SAWNUC [Lovejoy et al. 2004] and Yu [2005] for 52 % RH and 296 K. Bulk density ρ from CRC [1979], D_{mass} is mass diameter, k_f is the forward rate coefficient for addition of the doubly hydrated H_2SO_4 (SA) molecule indexed for product cluster. A fit of the volume of the clusters, V, as a function of # of SA molecules is: V / cm^3 = $1.276x10^{-22}(\#SA)^{1.115}$.

# SA	Pk. # W SAWNUC[a]	Fastest SA evap.[b]	# W, Yu [c]	wt.%	ρ / (g/cm^{-3})[d]	D_{mass} / nm	k_f / cm^{-3} s^{-1}	k_f / cm^{-3} s^{-1} 'old' [e]	D_c / atm cm^2 s^{-1} [f]
1	1.5	-	1.2	78.4	1.71	**0.62**	-	-	0.076
2	4	2	3	73.1	1.65	**0.80**	3.88E-10	4.95E-10	0.057
3	7	4.5	5	71.5	1.63	**0.93**	4.39E-10	5.47E-10	0.0493
4	10.5	7.5	8.5	96.6	1.61	**1.04**	4.92E-10	6.02E-10	0.0418
5	14	10.5	11	67.7	1.58	**1.14**	5.43E-10	6.55E-10	0.0368
6	17.5	14	14	65.8	1.56	**1.22**	5.91E-10	7.03E-10	0.0330
7	21	17.5		64.5	1.55	**1.30**	6.37E-10	7.49E-10	0.0302
8	25	21	21	63.5	1.54	**1.37**	6.80E-10	7.93E-10	0.0279
9	28.5	25		62.8	1.53	**1.43**	7.22E-10	8.34E-10	0.0260
10	32	28.5	28	62.6	1.52	**1.49**	7.62E-10	8.74E-10	0.0244
20	74	70	65	59.5	1.50	**1.92**	1.11E-09	1.21E-09	0.0159
30	120	115	105	57.6	1.47	**2.23**	1.40E-09	1.47E-09	0.0123
40	168	163	170	56.4	1.45	**2.48**	1.66E-09	1.71E-09	0.0102
50	217	212	195	55.6	1.44	**2.69**	1.89E-09	1.91E-09	0.00883
100	479	474	420	53.2	1.42	**3.46**	2.90E-09	2.78E-09	0.00557
150	755			52.0	1.41	**4.00**	3.76E-09	3.48E-09	0.00424
200	1042			51.1	1.40	**4.44**	4.53E-09	4.09E-09	0.00348
300	1631			50.5	1.39	**5.13**	5.91E-09	5.16E-09	0.00263
∞	*#W / #SA = 7.5 in the bulk*			42.1	1.32	-	-	-	-

[a] Most abundant hydrate, pseudo-steady state. [b] Hydrate with the largest SA evaporation rate. [C] The critical cluster for 50 % RH and 298 K, from Yu's Fig 2(a). [d] CRC [1970] for the bulk densities. [e] 'old': Hanson et al. [2019] also used the kinetic theory of McMurry [1980] but assumed the monomer and all clusters had the bulk composition: 42 wt. % or 7.5 H_2O per H_2SO_4. [f] Diffusion coefficient using Mason and Monchik [196x] with a collision integral factor ($\Omega_{1,1}$) = 1.24.

Model details and thermos.

The two phenomenological sets of cluster free energies considered here differ in their putative binary system thermodynamics. The NH3_52 and NH3_D52 binary system thermodynamics and that given by SAWNUC [Lovejoy et al., 2004, 2009] at 52% RH (transformed into quasi-unary by weighting over the water distribution to get an average equilibrium constant for addition of H_2SO_4) are compared in Fig.

S13. In the designation NH3_D52, D52 indicates the free energies for the zero-ammonia containing clusters while NH3_D52 designates the entire system (quasi-unary and quasi-binary) cluster free energies. Fig. S12 shows predicted N_p as a function of Q_4 for three quasi-unary (zero ammonia) free energy schemes. NH3_52 and SAWNUC for 52 % RH yield similar N_p while D52 is about an order of magnitude lower. The D52 binary thermodynamics predict N_p that are nearly identical to the experimental data from Figure 5 for Q_4 = 4.2 sccm and larger.

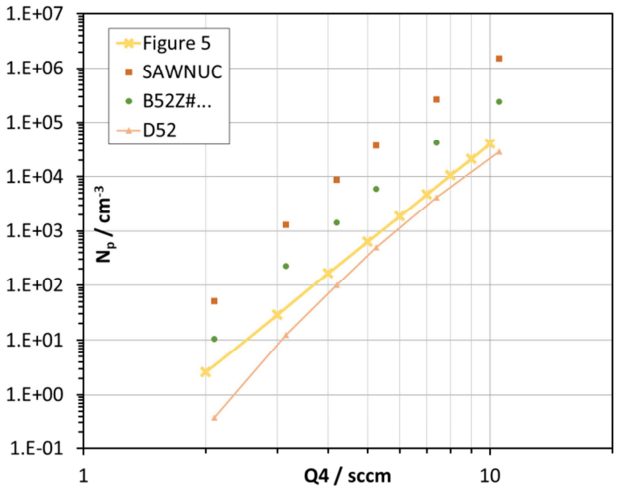

Fig. S12. Binary system, N_p vs. Q_4, modeled with three different thermodynamics. NO, NO_2 and HONO fractions were varied according to Figure 2. Thick yellow line representing lower envelope of experimental data in Figure 5.

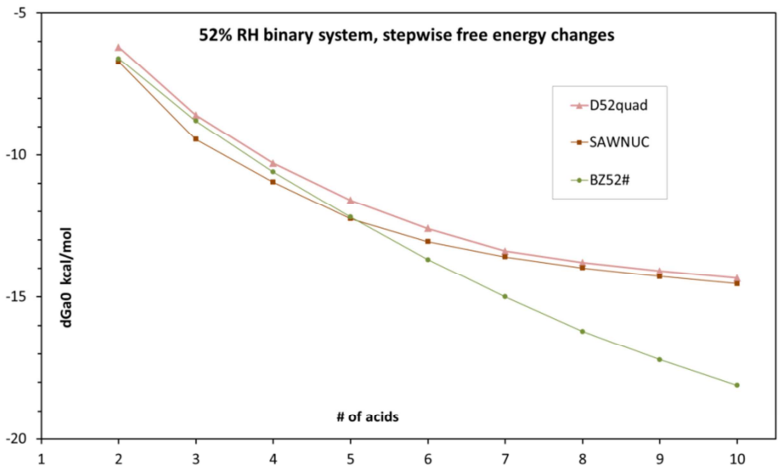

Fig. S13. Quasi-unary standard free energy changes for addition of H_2SO_4 (hydrated) to n-1 cluster as a function of product cluster, n. D52 is the binary set developed here, B52# is NH3_52 from Hanson et al. [2019] and SAWNUC is from Lovejoy et al. [2004]

Shown in Fig. S14 are the step-wise standard free energy changes for addition of an H_2SO_4 molecule, ΔG_a^0, for NH3_52 (thin lines) and NH3_D52 (thick lines). Product clusters are indexed with the number of H_2SO_4 molecules along the X-axis and number of ammonia molecules color-coded. These two schemes are close in ΔG_a^0 up to the 5 H_2SO_4 clusters; larger clusters (more NH_3 or more H_2SO_4) reveal that NH3_D52 has weaker bonding than does NH3_52, due in large part to the prescription that the large clusters with few ammonia molecules approach the quasi-unary free energy for the binary system.

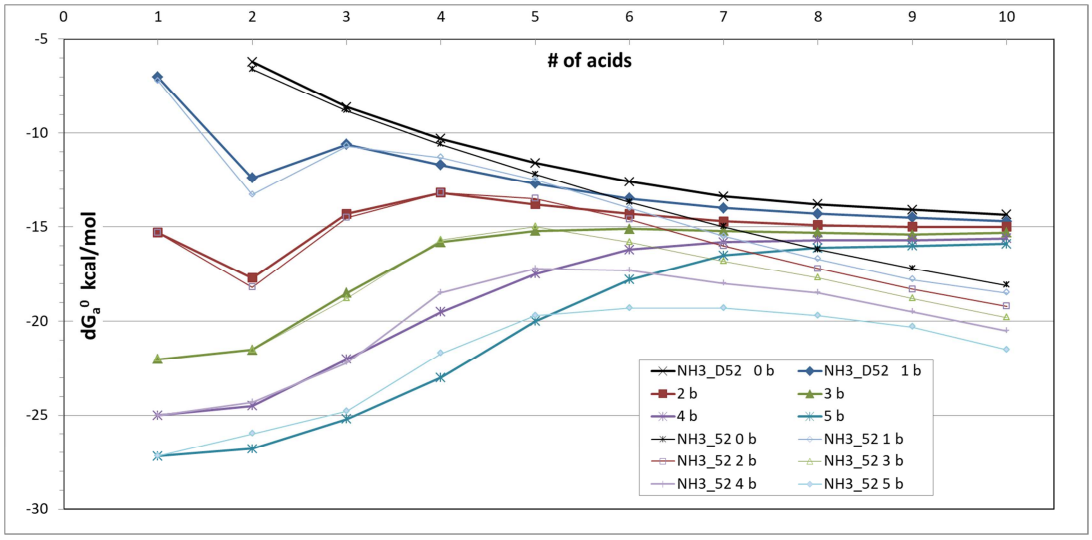

Fig S14. Comparison of NH3_D52 (thick lines) and NH3_52 (thin lines) thermodynamics, step-wise free energy changes for adding an acid molecule (binary is designated ' 0 b '). ΔG_a^0 for 1 acid binary is taken to be 0. The number of ammonia molecules in the cluster indicated by color.

Ion calculations and discussion.

The Froyd et al. data covers up to 6 H_2SO_4 ligand molecules on the bisulfate ion and also has energetics of hydration. We averaged over hydrates to obtain a quasi-unary equilibrium constant that yields the free energies for the negative ions. The forward rate coefficient was taken to be $2x10^{-9}$ cm^3 s^{-1} for all clusters. The quasi-unary free energies were extended to 9 H_2SO_4 ligands by assuming no changes in the stepwise ΔG. In the ion-mediated pathway, particles can also be formed when positive and negative ions recombine but for our conditions this was found to be negligible compared to the negative ion channel. Experimentally, these ions / charged particles will be affected / neutralized in the charger which will affect how the DEG system counts them while the UCPC system counts them regardless. The quasi-unary free energies for the negative ions are presented in the Table below.

n, # of H_2SO_4 ligands	ΔG^0, SAWNUC stepwise	Total standard free energy	Stepwise, bisulfate ion, Froyd et al.	Total, ion
0	-	0	-	-
1	-6.72	-6.72	-23.02	-23.02
2	-9.46	-16.17	-17.03	-40.05
3	-10.96	-27.14	-13.84	-53.88
4	-12.26	-39.40	-11.70	-65.58
5	-13.06	-52.46	-12.62	-78.20
6	-13.60	-66.06	-13.08	-91.28
7	-13.99	-80.04	-13	-104.28
8	-14.29	-94.33	-13	-117.28
9	-14.54	-108.88	-13	-130.28

Quasi-unary Gibbs energies at 296 K and 52% RH. Ion energies from Froyd et al.. SAWNUC (modified liquid drop) energies from Lovejoy et al. [2004]. n is that in (HSO_4^-). $(H_2SO_4)_n$ or $H_2SO_4.(H_2SO_4)_n$.

N_p and mode diameter vs. Q_4 over time.

Shown in Fig S15 are the leading edge particles number density N_p and diameter vs. Q_4. The data has been split into four time periods to illustrate the change over time in the relationship between the measurements and Q_4. The 2018 May and June data were included in the Hanson et al. [2019] data set (a $Q_4^{3.5}$ power relationship is shown), the 29Jun to 28Sep 2018 data overlaps the earlier data, while the data later in 2018 definitely departs to lower values of N_p for all Q_4. Although the mode diameter data is somewhat scattered, there is not a temporal trend thus particle growth was constant over time, suggesting HONO and NO levels at a given Q_4 were also constant.

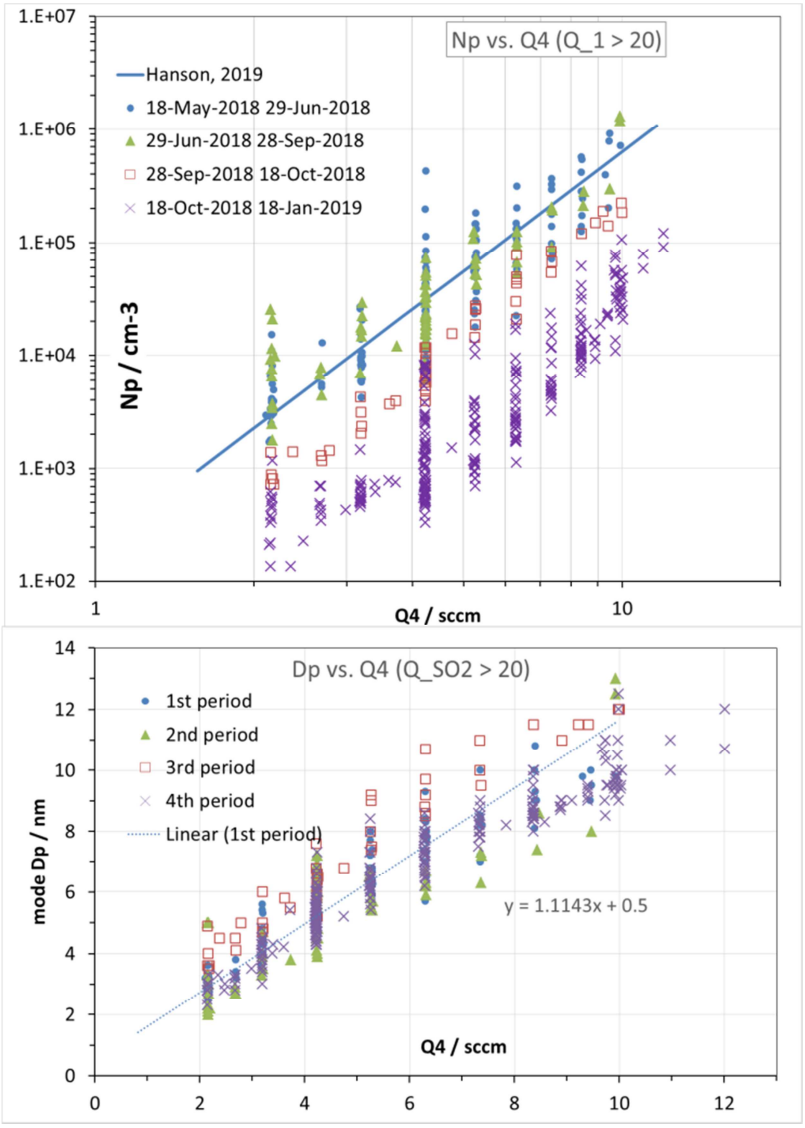

Fig. S15. Particle characteristics of the leading edge mode from the DEG system vs. Q_4, (a) Np and (b) mode diameter.

NH3_D52 Gibbs energies and enthalpies for H_2SO_4-NH_3 clusters at 52 % RH.

Cluster Gibbs energies (298 K) as a function of # of sulfuric acids (columns) and # of ammonias (rows), kcal/mol.

	0	1	2	3	4	5	6	7	8	9	10
0	0	0	-6.2	-14.8	-25.1	-36.7	-49.3	-62.7	-76.5	-90.6	-104.95
1	0	-7	-19.4	-30	-41.7	-54.4	-67.9	-81.9	-96.2	-110.7	-125.4
2	4	-11.3	-29	-43.3	-56.5	-70.3	-84.6	-99.3	-114.2	-129.2	-144.2
3	8	-14	-35.5	-54	-69.8	-85	-100.1	-115.3	-130.6	-146	-161.3
4	9.5	-15.5	-40	-62	-81.5	-99	-115.2	-131	-146.7	-162.4	-178
5	10.7	-16.5	-43.3	-68.5	-91.5	-111.5	-129.3	-145.8	-161.9	-177.9	-193.8
6	11.9	-17.5	-46	-73.6	-99	-121.9	-142	-159.8	-176.7	-193	-209.3

Enthalpies (kcal/mol) as a function of # of sulfuric acids (columns) and # of ammonias (rows)

	0	1	2	3	4	5	6	7	8	9	10
0	0	0	-16.3	-37.3	-59.8	-83.8	-108.8	-134.8	-161.8	-189.8	-218.8
1	0	-14	-40	-63.5	-87	-111	-136	-162.0	-189.0	-217.0	-246.0
2	0.4	-26	-57	-86	-112	-137	-163	-189.5	-217.0	-245.5	-275.0
3	-4.4	-36	-73	-106.5	-136	-161	-187	-215.0	-244.0	-272.5	-302.0
4	-8.3	-46.3	-85	-122	-156	-183	-210	-238.0	-267.0	-297.0	-327.0
5	-12.2	-53	-94	-134	-171	-203	-232	-261.0	-291.0	-321.0	-352.0
6	-16.1	-59.5	-101.5	-144	-183	-220	-252	-282.0	-313.0	-344.0	-376.0

References not in main text:

Handbook of Chemistry and Physics, 35th edition, Hodgman, C.S., Weast, R.C., Wallace, C.W. editors, Chemical Rubber Publishing Co., Clevelend, OH, 1953-1954.

Larriba, A., Hogan, C. and de Lamora, J.: The Mobility–Volume Relationship below 3.0 nm Examined by Tandem Mobility–Mass Measurement, Aerosol Science and Technology, 45, 453-467, 2010.

Monchick, L.; Mason, E. A. The Transport Properties of Polar Gases. J. Chem. Phys. 1961, 35, 1676.

Mason, E. A.; Monchick, L. Transport Properties of Polar-Gas Mixtures. J. Chem. Phys. 1962, 36, 2746.

Nieminen, T., Lehtinen, K. E. J. and Kulmala, M.: Sub-10 nm particle growth by vapor condensation – effects of vapor molecule size and particle thermal speed, Atmos. Chem. Phys., 10(20), 9773–9779, doi:10.5194/acp-10-9773-2010, 2010.